Experimental Mechanics (2006) 46: 91–103
DOI 10.1007/s11340-006-5862-5

RESEARCH PAPER

# A Transparent Indenter Measurement Method for Mechanical Property Evaluation

**C. Feng · B.S.-J. Kang**

Received: 15 August 2005 / Accepted: 13 October 2005


**Abstract** An optical Transparent Indenter Measurement (TIM) method was developed for measurement of material surface mechanical properties. During the spherical indentation test, *in-situ* measurements of indentation-induced surface out-of-plane displacements were obtained using an integrated phase-shifting Twyman-Green interferometer. Based on elastic recovery theory and 2D finite element analyses, a procedure was developed to determine the material Young's modulus using the measured surface out-of-plane displacements. During the spherical indentation test, contact radii were also measured and used to estimate the material post-yielding true stress-strain curve using Tabor's empirical relation. An experimental TIM apparatus was assembled to test on two engineering alloys and the results showed good agreement with known material properties.

**Keywords** Transparent indenter measurement · Spherical indentation · Young's modulus · Out-of-plane displacement · Stress-strain curve

## Introduction

Since Tabor [1] showed the application of spherical indentation approach to obtain material post-yielding true stress-strain curve, spherical indentation technique has been applied to determine material mechanical properties such as Young's modulus and post-yielding behavior [2–18, 20–23]. The indentation parameters such as load, indentation depth, contact radius and unloading characteristics have been studied extensively either experimentally or numerically [1–25]. In the early 1970s, with the work of Sneddon, Bulychev et al [2, 3], unloading stiffness method was successfully used to measure material Young's modulus. Later, it was extended to brittle material with depth-sensing Vickers indentation by Loubet [4]. Doerner and Nix [5] studied the unloading characteristics using instrumented indentation. Oliver and Pharr [6] studied the unloading behavior of six different materials, and concluded that, instead of a straight line, the unloading load-depth curve actually has a similar power law form to that of the loading-depth curve. Therefore, only initial unloading stiffness is suitable for the Young's modulus determination. With the development of various thin film materials, depth-sensing indentation is often applied to evaluate mechanical properties of thin film materials [6, 9, 11, 13–15].

However, indentation test is a complicate mechanical process. It involves complex contact mechanics and nonlinear plastic deformation. Analytical solutions are difficult to obtain. As a result, much of the understanding of the indentation process has been acquired through experiments and finite element analyses. Thus accurate experimental measurement of indentation parameters is critical in determining material surface mechanical properties using indentation technique. With the advancement of computational mechanics, fully elastic-plastic finite element analyses have provided further understanding of indentation process. From finite element analyses, indentation parameters, such as loading-unloading characteristics, surface deformation, stress distribution and elastic

C. Feng (SEM member) · B.S. Kang (✉, SEM member)
Mechanical and Aerospace Engineering Department,
West Virginia University, Morgantown, WV 26506, USA
e-mail: bruce.kang@mail.wvu.edu

recovery can be analyzed to study the indentation process for both bulk and thin film materials. 2D finite element analyses [7–15] were often used for simulating axisymmetric indentation process, and 3D analyses were used for more complicated and general cases [15–18].

Since indentation unloading is elastic, direct surface displacement measurement of the unloading elastic recovery can potentially be used to obtain the material mechanical properties. However, to the best of our knowledge, no such experimental work has been reported in the literature. Experimental measurements of indentation-induced deformation were only carried out for residual fields. As early as in the 1930s, Nadai [19] showed different deformation modes after a cylindrical punch. In the 1970s, Underwood [20] applied optical interferometric method to study the residual out-of-plane deformation and correlated to residual stress of the specimen prior to indentation tests. Szutkowska [21] studied the fracture toughness, deformation and hardness by Vickers indentation without further analyses. Alcala et al [22] correlated piling-up and sinking-in to material uniaxial strain hardening exponent $n$ by studying residual indent profiles. Sub-surface deformation was also experimentally studied to estimate the stress-strain distribution underneath the indentation using bonded-interface or sectioning method [15].

It should be noted that to quantify the post-yielding stress-strain data using Tabor's empirical relation [equation (1a) and (1b)] [1], accurate measurements of indentation contact radius and applied load are necessary.

$$\varepsilon = 0.2\frac{d}{D} \tag{1a}$$

$$\sigma = \frac{P_m}{C} \tag{1b}$$

$$P_m = \frac{Load}{\pi a^2} \tag{1c}$$

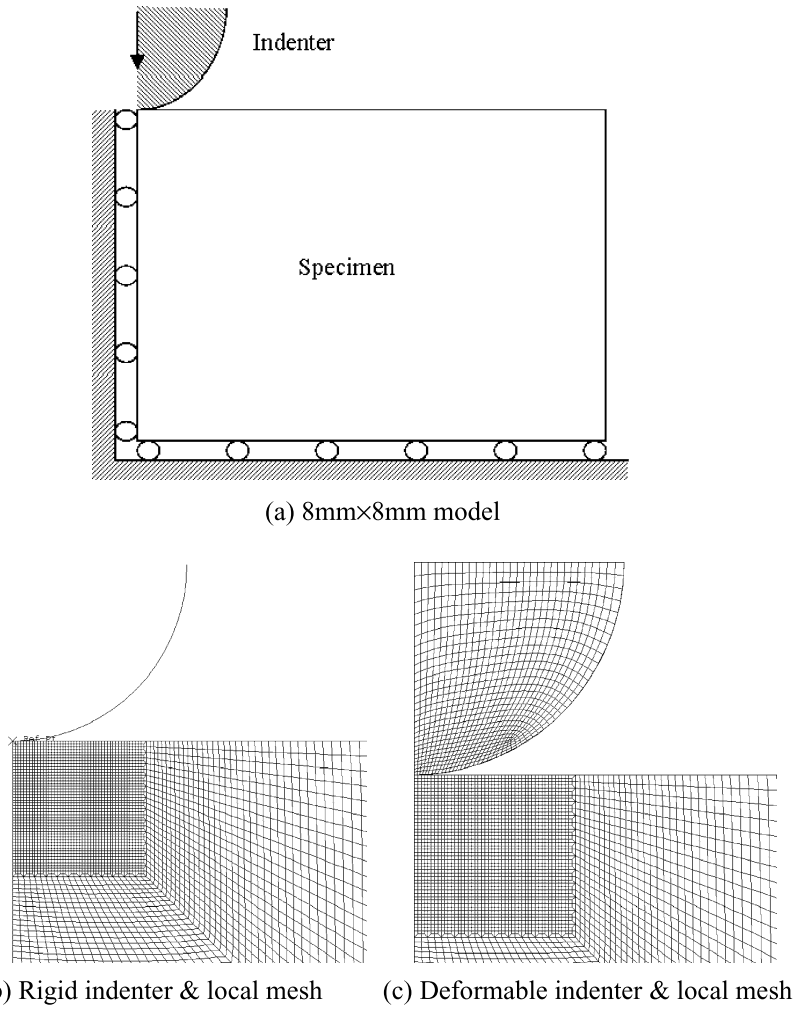


(a) 8mm×8mm model

(b) Rigid indenter & local mesh

(c) Deformable indenter & local mesh

**Fig. 1.** Axisymmetric 2D FEA model

**Table 1** Material matrix for FEA

| Specimen(IN783) | Indenter |
|---|---|
| E=177.3 GPa<br>$\sigma_y$ = 779 MPa<br>$\sigma_{ult}$ = 1194 MPa (20%strain)<br>$\nu$=0.31 | Rigid indenter<br>Deformable indenter<br>(BK7 optical glass)<br>E=81 GPa<br>$\nu$=0.206 |

where σ and ε are the post-yielding true stress and strain, $d$ is the contact diameter, $D$ is the indenter diameter, $P_m$ is the mean pressure and $C$ is the constraint factor.

In a load-depth sensing indentation, indirect estimation of the contact radius has been carried out using load-depth data. To construct the post-yielding data points, multiple loading-unloading processes are generally involved and certain assumption of the material properties and specific material parameters must be assigned [23]. Thus far, direct contact radius measurement is only applicable to residual indentation fields for the case of spherical indentation. As for the constraint factor, $C$, it has been shown that $C$ = 2.8 works quite well for steel and copper alloys [1], but for other alloys, different $C$ values ranging from 2.45 to 3.1 were suggested depending on the material strain hardening property [7, 15, 22, 23].

In this research, a new experimental method, Transparent Indenter Measurement (TIM), which is capable of real-time *in-situ* surface out-of-plane displacement and direct contact radius measurements, was developed to evaluate material surface mechanical properties based on spherical indentation. During the indentation test, *in-situ* measurement of out-of-plane displacements was carried out using phase-shifting Twyman-Green interferometry. Using elastic recovery theory and 2D finite element simulation, a procedure was developed to determine material Young's modulus based on the measured out-of-plane displacements. The transparent indenter design also allows for direct measurement of contact radius which is then used to estimate the post-yielding true stress-strain data based on equation (1).

## Elastic Recovery and Finite Element Analysis

### Elastic Recovery and Evaluation of Young's Modulus

Since indentation unloading is an elastic process, the elastic solution based on contact mechanics is applicable to characterize the unloading process. For indentations on pure elastic materials, both flat-end punch and spherical indentation solutions are available.

For flat-end punch, elastic surface out-of-plane displacement, $w$, under load $P$ is described as [2],

$$w(\rho) = \frac{1-\nu^2}{E}\frac{P}{\pi a}\sin^{-1}\left(\frac{a}{\rho}\right), \rho > a \tag{2}$$

For spherical indentation [24, 25],

$$w(\rho) = \frac{3}{4}\frac{1-\nu^2}{E}\frac{P}{\pi a^3}\left[\left(2a^2-\rho^2\right)\sin^{-1}\left(\frac{a}{\rho}\right) + a\sqrt{\rho^2-a^2}\right], \quad \rho > a \tag{3}$$

Where $a$ is the contact radius and $\rho$ is the distance to the indentation center.

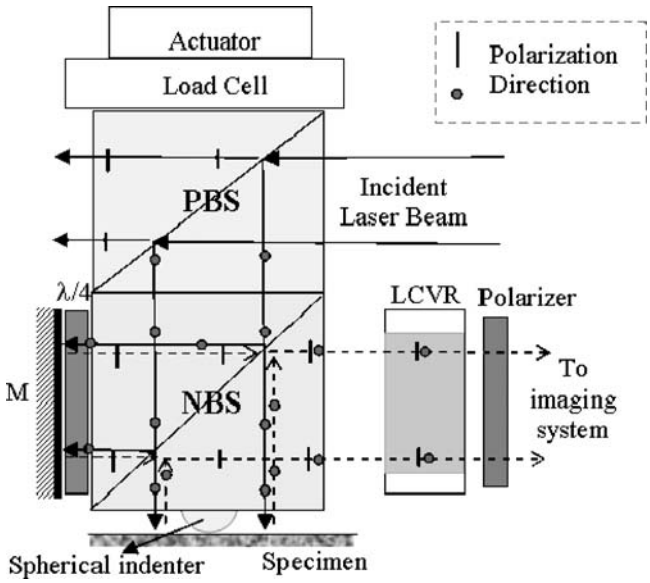


**Fig. 2.** Schematic optical layout of the Through Indenter Measurement (TIM) system. PBS: Polarization cubic beam-splitter; NBS: Non-polarization cubic beam-splitter; LCVR: Liquid crystal variable retarder; M: Reference mirror; λ/4: quarter waveplate

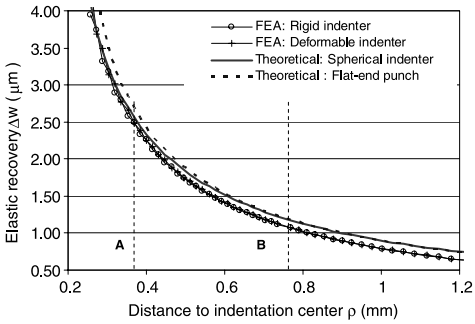


(a) Comparison of elastic recovery $\Delta w$

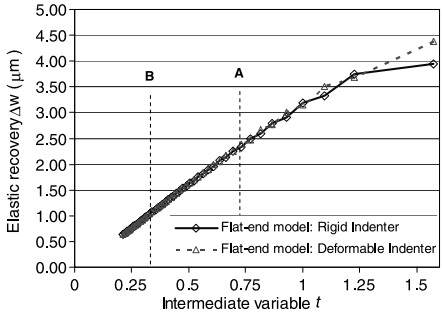


(b) $\Delta w \sim t$ relation using flat-end punch model

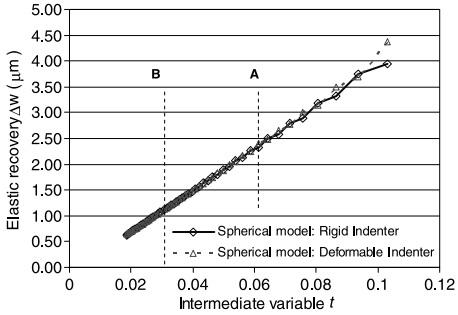


(c) $\Delta w \sim t$ relation using spherical indenter model

**Fig. 3.** FEA elastic recovery, A = 1.5 $a$= 0.384 mm, B = 0.768 mm, $P_{max}$ = 550 N, $P_{min}$ = 0

For an elastic-plastic indentation test, the distribution of unloading-induced elastic recovery ($\Delta w$) can be modeled by either flat-end punch or spherical indentation model.

For the flat-end punch model,

$$\Delta w(\rho) = \frac{1-\nu^2}{E}\frac{\Delta P}{\pi a}\sin^{-1}\left(\frac{a}{\rho}\right), \rho > a \tag{4}$$

For the spherical indentation model,

$$\Delta w(\rho) = \frac{3}{4}\frac{1-\nu^2}{E}\frac{P}{\pi a^3}\left[\left(2a^2-\rho^2\right)\sin^{-1}\left(\frac{a}{\rho}\right) + a\sqrt{\rho^2-a^2}\right], \quad \rho > a \tag{5}$$

From equations (4) and (5), Poisson's ratio and Young's modulus are the only two mechanical properties involved. Young's modulus can be calculated from the elastic recovery distribution if Poisson's ratio is known. By re-writing equations (4) and (5), both models can be transformed into a linear relationship using an intermediate variable $t$,

$$\Delta w(t) = mt + \mathrm{b} \tag{6}$$

Where for flat-end punch,

$$t = \sin^{-1}\left(\frac{a}{\rho}\right) \tag{7a}$$

$$m = \frac{1-\nu^2}{E}\frac{P}{\pi a} \tag{8a}$$

And for spherical indentation,

$$t = \left[\left(2a^2-\rho^2\right)\sin^{-1}\left(\frac{a}{\rho}\right) + a\sqrt{\rho^2-a^2}\right] \tag{7b}$$

$$m = \frac{3}{4}\frac{1-\nu^2}{E}\frac{P}{\pi a^3} \tag{8b}$$

The variable $b$ in equation (6) is used to compensate the rigid body motion in experimental data.

By converting experimental $\Delta w \sim \rho$ data to $\Delta w \sim t$ relation, $m$ can be calculated from linear curve fitting of the $\Delta w \sim t$ data. Then using measured load $P$ and

**Table 2** Error % of Young's modulus calculation, FEA

| | Rigid indenter | Deformable indenter |
|---|---|---|
| Flat-end model | ≤0.6% | ≤3.3% |
| Spherical model | ≤0.2% | ≤1.7% |

**Fig. 4.** Indenter of TIM system

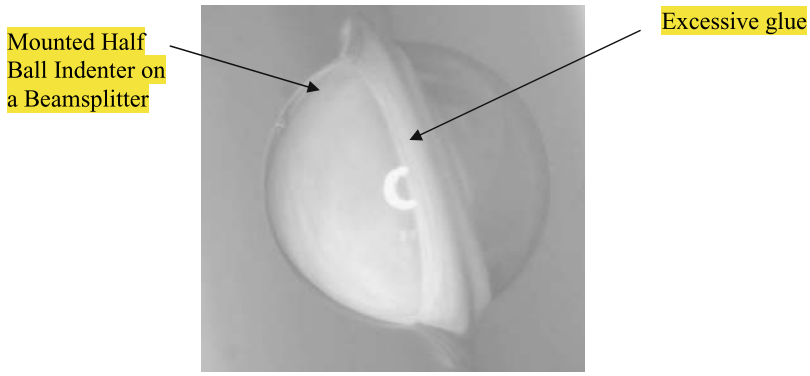


(a) 3D view of a mounted indenter

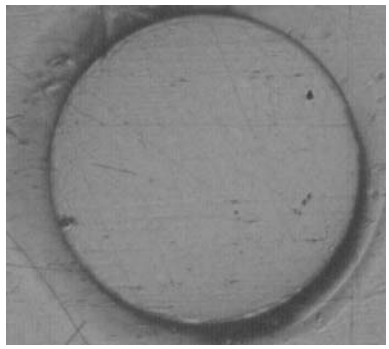

(b) Through indenter view, white light illumination

**Fig. 5.** Initial fringe pattern in TIM system

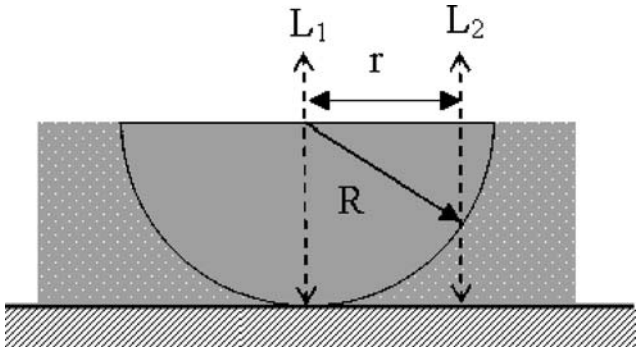


(a) Indenter in index matching fluid

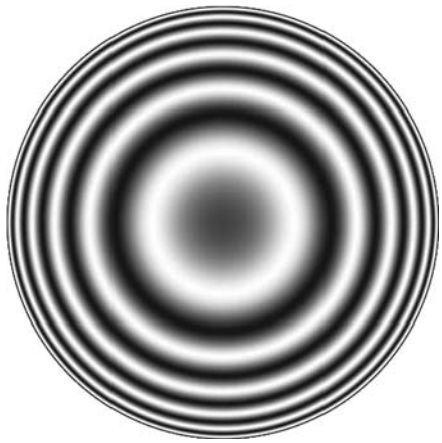

(b) Theoretical initial fringe patterns

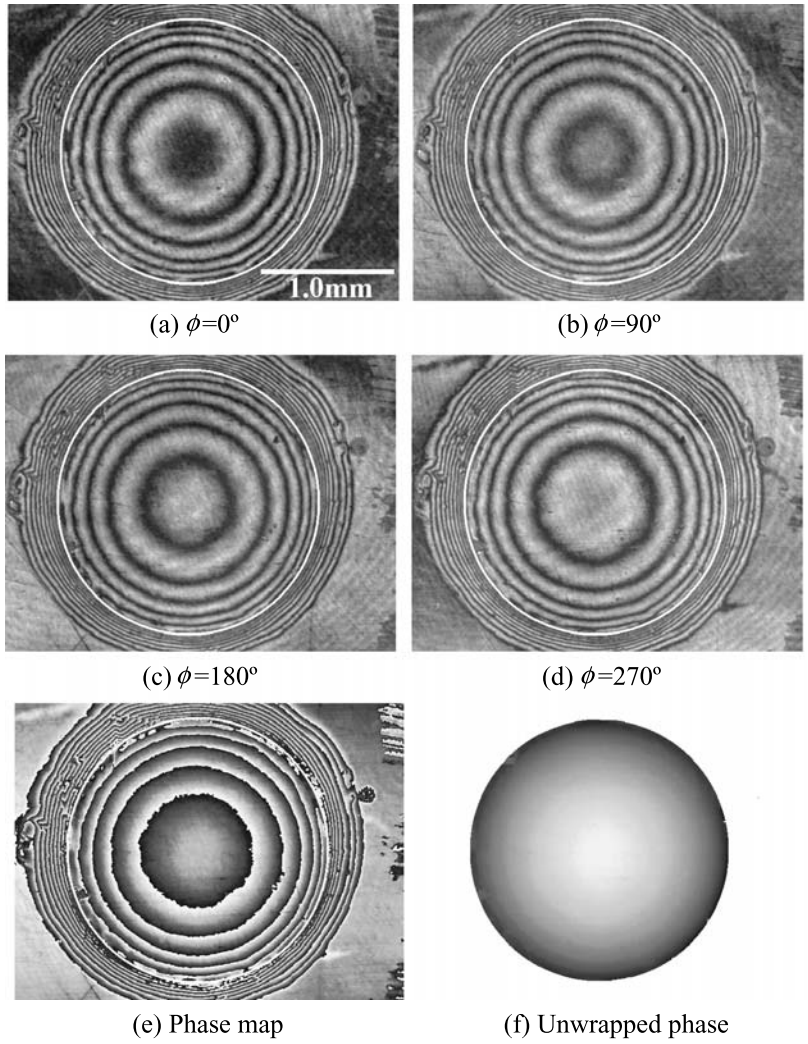


**Fig. 6.** Typical TIM system initial fringe patterns

contact radius, $a$, the Young's modulus can be determined by re-writing equation (8a) and (8b).

$$E = \left(1-\nu^2\right)\frac{P}{\pi a}\frac{1}{m}\,(\text{flat-end punch}) \tag{9a}$$

$$E = \frac{3}{4}\left(1-\nu^2\right)\frac{P}{\pi a^3}\frac{1}{m}\,(\text{spherical indentation}) \tag{9b}$$

Finite Element Analyses

A series of elastic-plastic finite element analyses were conducted to investigate indentation elastic recovery and develop procedures for Young's modulus calculation. Figure 1(a) shows the 8 mm × 8 mm axisymmetric 2D model with 2 mm-diameter indenter. General purpose finite element software package ABAQUS™ was chosen to carry out all simulations. Both rigid and deformable indenters were considered to study the effect of indenter rigidity on elastic recovery. Figure 1(b) and (c) show the finite element mesh design which consists of 6481 axisymmetric four-node linear quadrilateral elements. Reduced integration was chosen and ABAQUS™ has built-in hourglass control for the chosen type of element. Table 1 shows the material matrix used in all simulations. The materials are IN783 superalloy [28] as substrate and optical glass BK7 as indenter material.

## Experimental Program

Transparent Indenter Measurement (TIM) Method

Figure 2 shows the optical principle of the TIM method of which Twyman-Green interferometer and spherical indentation are integrated together. A 2 mm-diameter transparent indenter is attached to a non-polarizing cubic beam splitter. The two stacked cubic beam splitters are used to transfer load, incident light and capture images during the indentation test.

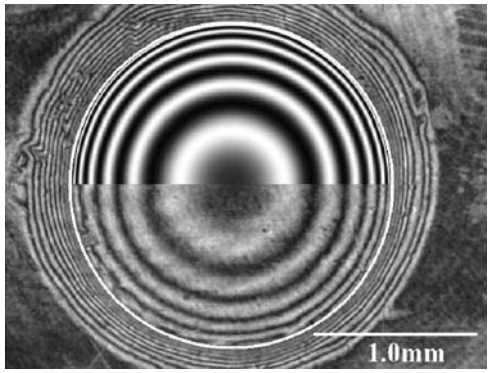


**Fig. 7.** Comparison of experimental and theoretical initial fringe patterns

The integrated Twyman-Green interferometer [26] is used to directly measure indentation-induced surface out-of-plane displacements. By introducing phase shifting technique, the measurement spatial resolution is further enhanced. As shown in Fig. 2, the beam incidented to the specimen has the polarization direction perpendicular to the paper and is reflected back to the imaging system. The reference beam passes through a quarter waveplate twice, thus the polarization direction is changed 90 degree. These two beams are now mutually perpendicular. Phase shifting is introduced as these two mutually perpendicular beams entering the liquid crystal variable retarder (LCVR). A polarizer is used to view fringe pattern in the imaging system [27]. Phase-shifting technique is used to improve the fringe measurement resolution and accuracy [29].

## Test Procedures

A typical TIM test involves two loading-unloading procedures at the same indentation spot. The first loading-unloading is aimed to measure Young's modulus, and the second is aimed to establish post-yielding stress-strain data.

At the first loading-unloading, a small load is applied and the *in-situ* out-of-plane displacement is measured. Then the load is released and the corresponding *in-situ* residual out-of-plane displacement is measured. From the two measured out-of-plane displacements, Young's modulus is calculated following the procedure described earlier. After the first loading-unloading procedure, a sequence of monotonically increasing loads is applied at the same indented location. Here the measurement is focused on the post-yielding stress-strain data. Using TIM method, contact radii and applied loads are measured incrementally to obtain sufficient data which are then used to establish the post-yielding stress-strain data using Tabor's empirical relation, i.e., equation (1a) and (1b).

## Test Alloys

Experiments were done on two materials, IN783 and Al6061-T0. Initial residual stress is assumed negligible for both alloys. The IN783 superalloy had standard heat treatment (1120°C/1 hr/AC + 845°C/8 hrs/AC + 720°C/8 hrs 50°C/hr 620°C/8 hrs/AC). A simplified bi-linear stress-strain curve as shown in Table 1 [28] is

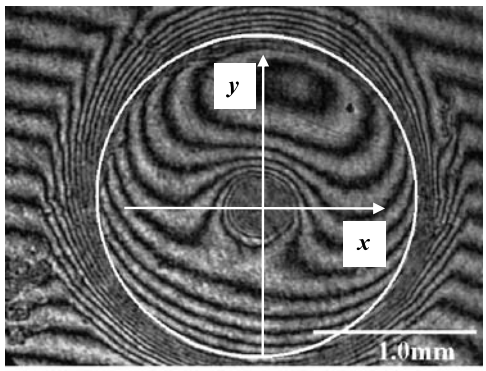


(a) Fringe pattern with carrier

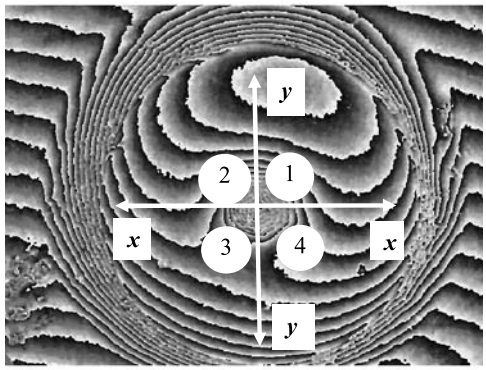


(b) Corresponding phase map

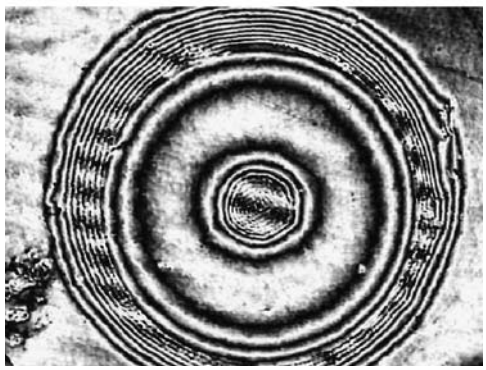

(c) Generated fringes with carrier removed numerically from (b)

**Fig. 8.** Inclination problem during indentation loading and unloading

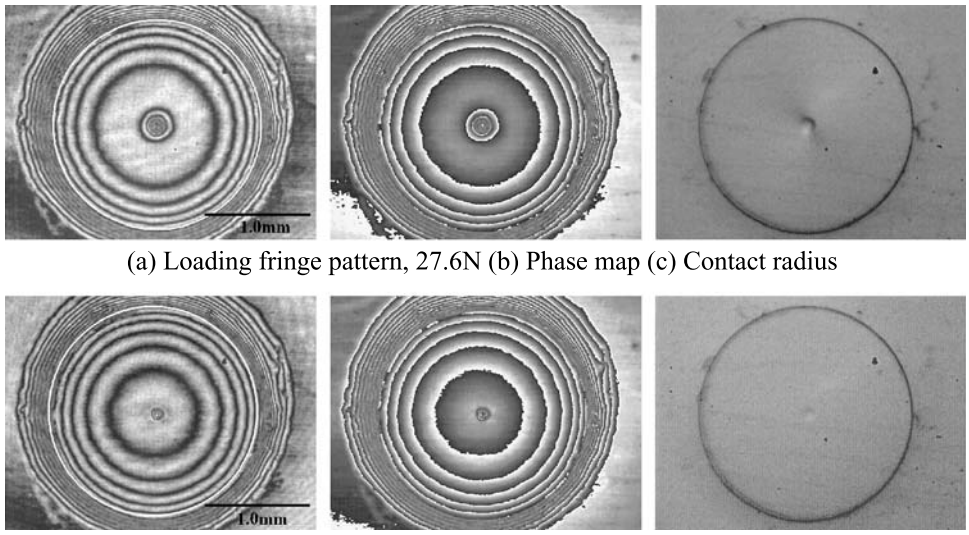


**Fig. 9.** Indentation of IN783 superalloy

(a) Loading fringe pattern, 27.6N (b) Phase map (c) Contact radius

(d) Unloading fringe pattern (e) Phase map (f) Contact radius

used for the elastic-plastic finite element indentation simulations. Standard tension tests were conducted on the Al6061-T0 alloy to obtain the stress-strain curve which is determined to be $\sigma = 205\varepsilon^{0.2}$ (MPa) with Young's modulus of 69GPa and Poisson's ratio of 0.33.

## Results

### Validation of Young's Modulus Measurement

Figure 3(a) shows comparative results of elastic recovery ($\Delta w$) between finite element analyses and theoretical solutions. For both spherical and flat-end punch solutions, the finite element results matched well with the analytical solutions except very near the contact boundary where the difference is noticeable. This is expected that, due to large plastic deformation, the region near the contact radius may deform irregularly [19, 20]. Converting $\Delta w \sim \rho$ relation to $\Delta w \sim t$ relation using equation (7a) and (7b), the linearity showing in Fig. 3(b) and (c) indicates the region of validity (i.e., From A to B as shown in Fig. 3(a)) of using the elastic recovery solution for Young's modulus determination. Specifically, the Young's modulus is calculated using equation (9a) and (9b) where $m$ is the slope of the linear portion of the $\Delta w \sim t$ plot between A and B in Fig. 3. Table 2 shows the errors for both flat-end and spherical models are all less than 5%.

### Initial Adjustment of TIM System

As shown in Fig. 4(a), a 2 mm-diameter transparent indenter is attached to a cubic beam splitter. The

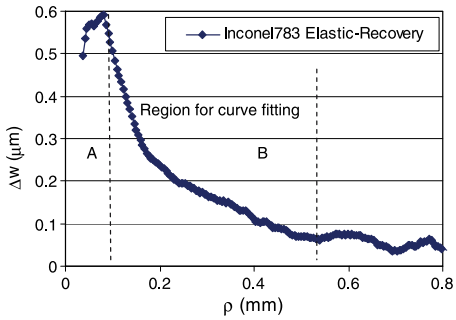


(a) Elastic recovery

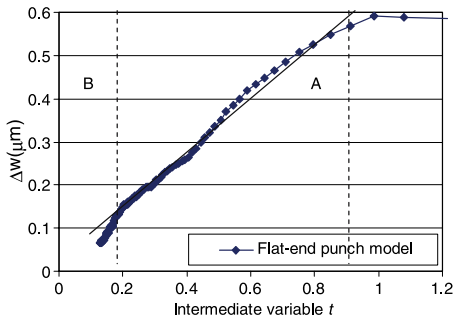


(b) $\Delta w \sim t$ relation in flat-end punch model

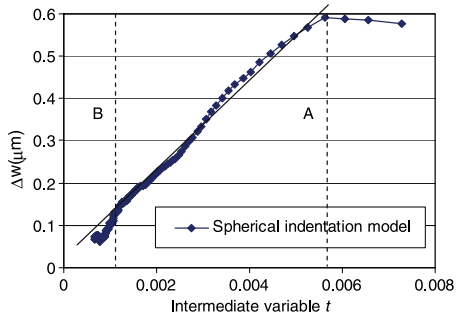


(c) $\Delta w \sim t$ relation in spherical model

**Fig. 10.** Experimental elastic recovery and $\Delta w \sim t$ relation for IN783

**Table 3** Error % of Young's modulus calculation, Experimental

| | IN783 (177.3GPa) | | Al 6061-T0 (69GPa) | |
|---|---|---|---|---|
| | Average | Max. error | Average | Max error |
| Flat-end model | 187.0 GPa | ≤6% | 72.6 GPa | ≤6% |
| Spherical model | 174.5 GPa | ≤5% | 70.3 GPa | ≤4% |

excessive glue around the indenter edge (corona) will cause the formation of irregular fringes around the indenter. While conducting indentation test using the indenter, the gap between the indenter and specimen surface is filled with index matching fluid. Figure 4(b) shows the through indenter view using white light illumination.

The index changing rate of matching fluid is approximately 0.0004/°C. Without strict temperature control, initial fringe pattern is inevitable. However, using phase-shifting technique, this initial fringe pattern can be easily subtracted. The formation of the initial fringe patterns is discussed below.

As shown in Fig. 5(a), the relative optical path difference (OPD) between $L_1$ and $L_2$ is,

$$\begin{aligned} \mathrm{OPD}_{initial} &= 2 \\ &\times \left( n_{Indenter}\sqrt{R^2 - r^2} + n_{index\_fluid}\left(R - \sqrt{R^2 - r^2}\right)\right) \\ &- 2 \times n_{Indenter} R \end{aligned} \tag{10}$$

Figure 5(b) shows numerically generated fringe patterns using equation (10) for a 2 mm-diameter BK7 indenter with $n_{BK7} = 1.51509$ (at wavelength 632.8 nm), and the index matching fluid, $n_{index\_fluid} = 1.5171$ (at wavelength 632.8 nm and 15°C).

Using TIM method, initial (no load applied) phase-shifted fringe patterns are shown in Fig. 6(a) to (d). Figure 6(e) and (f) show the corresponding phase map and unwrapped phase map. The outer denser irregular fringes are due to the excessive optical glue, as showed in Fig. 4(a). Also shown in Fig. 6, the white circle denotes the 2 mm-diameter indenter boundary.

Figure 7 shows comparison between experimental and theoretical initial fringe patterns, which shows good agreement in the central region (about 80% of the indenter radius $R$).

The initial fringe patterns will be superimposed to the indentation-induced out-of-plane displacement at each loaded stage. However, for Young's modulus measurement, the initial fringe patterns are automatically canceled out, this is explained in the following.

Upon applying load, due to the out-of-plane displacement, total OPD becomes,

$$\begin{aligned} \mathrm{OPD}_{Loading} &= 2 \times n_{index\_fluid} \times w_{Loading} \\ &+ \mathrm{OPD}_{initial} \end{aligned} \tag{11}$$

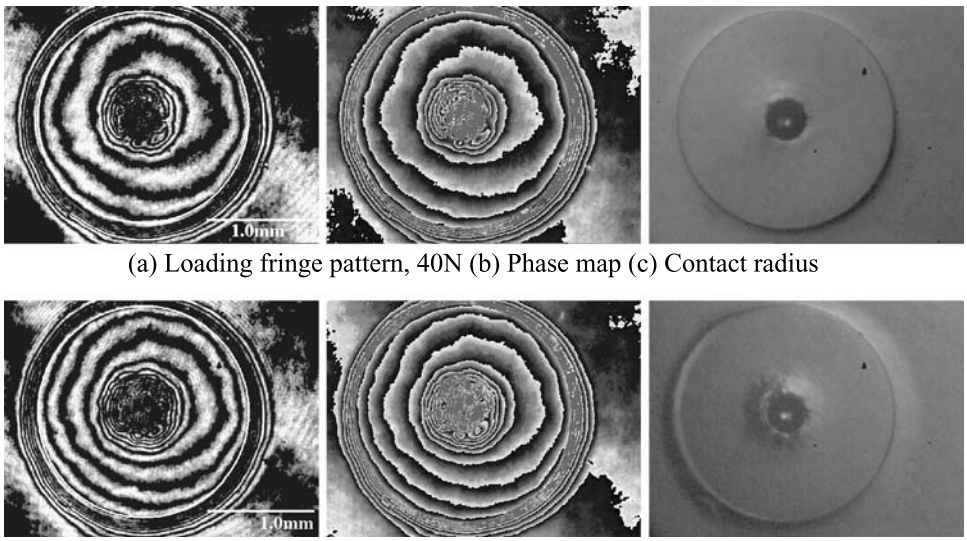


**Fig. 11.** Indentation of Al6061-T0

(a) Loading fringe pattern, 40N (b) Phase map (c) Contact radius

(d) Unloading fringe pattern (e) Phase map (f) Contact radius

After unloading,

$$\mathrm{OPD}_{UnLoading} = 2 \times n_{index\_fluid} \times w_{unloading} + \mathrm{OPD}_{initial} \quad (12)$$

Subtracting equation (11) from equation (12), relative change of OPD is,

$$\Delta\mathrm{OPD} = 2 \times n_{index\_fluid} \times \left(w_{unloading} - w_{Loading}\right) \quad (13)$$

and the elastic recovery is,

$$\Delta w = \frac{\Delta\mathrm{OPD}}{2 \times n_{index\_fluid}} \quad (14)$$

## Automatic Cancellation of Carrier Fringes

During loading, the specimen or indenter may be slightly tilted due to loading frame rigidity and specimen mounting. Therefore, the fringes will no longer be symmetric, as typically shown in Fig. 8. There are two approaches to solve this problem. One is to adjust the reference mirror to restore the symmetry. Another is to use the axisymmetric feature of the indenter to automatically cancel out the inclination-induced asymmetric carrier fringes. During indentation test, it is difficult to make accurate alignment to minimize carrier fringes. Usually, one or half carrier fringe pattern will be present. Therefore, it is also necessary to find a procedure to correct this carrier effect.

Based on the coordinate system in Fig. 8(a), the carrier-induced artificial displacements are,

$$w = w_{real} + a_L x + b_L y + c_L \quad (15)$$

Based on the coordinate system in Fig. 8(b), the corresponding displacement fields in quadrant 1 to 4 can be described as,

$$w_{q1\_L} = w_L + a_L x + b_L y + c_L \quad (16)$$

$$w_{q2\_L} = w_L - a_L x + b_L y + c_L \quad (17)$$

$$w_{q3\_L} = w_L - a_L x - b_L y + c_L \quad (18)$$

$$w_{q4\_L} = w_L + a_L x - b_L y + c_L \quad (19)$$

After unloading, the carrier coefficient $a$, $b$ and $c$ may be different, i.e.,

$$w_{q1\_u} = w_u + a_u x + b_u y + c_u \quad (20)$$

$$w_{q2\_u} = w_u - a_u x + b_u y + c_u \quad (21)$$

$$w_{q3\_u} = w_u - a_u x - b_u y + c_u \quad (22)$$

$$w_{q4\_u} = w_u + a_u x - b_u y + c_u \quad (23)$$

Subtracting equations (20–23) by equations (15–19), and adding together,

$$\Delta w_{q1} + \Delta w_{q2} + \Delta w_{q3} + \Delta w_{q4} = 4\Delta w + 4\Delta c \quad (24)$$

The elastic recovery can be written as,

$$\Delta w = \frac{1}{4}\left(\Delta w_{q1} + \Delta w_{q2} + \boldsymbol{w}_{q3} + \Delta w_{q4}\right) - \Delta c \quad (25)$$

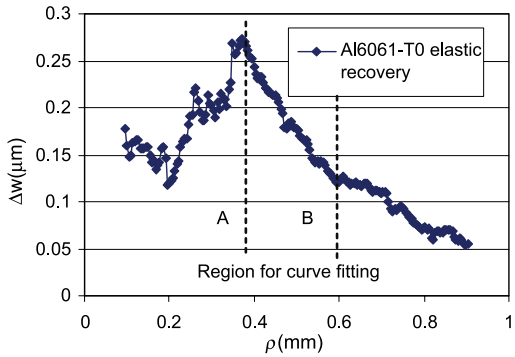


(a) Elastic recovery

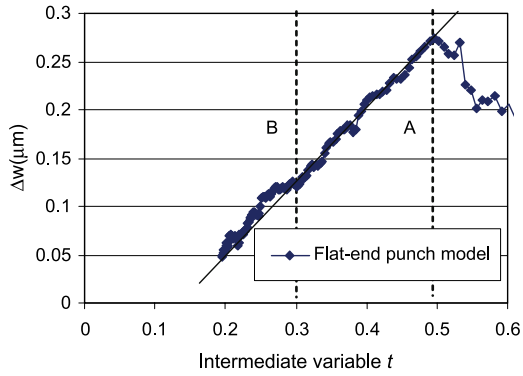


(b) $\Delta w \sim t$ relation in flat-end punch model

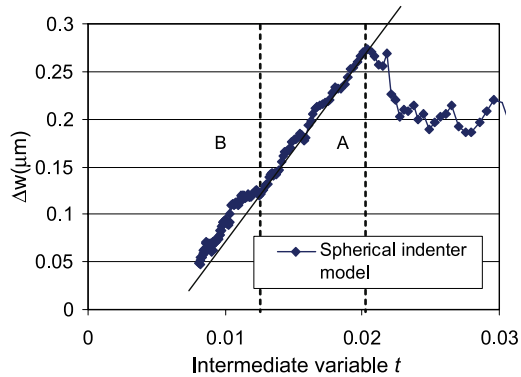


(c) $\Delta w \sim t$ relation in spherical model

**Fig. 12.** Experimental elastic recovery and $\Delta w \sim t$ relation for Al6061-T0

**Fig. 13.** Post-yielding results for IN783

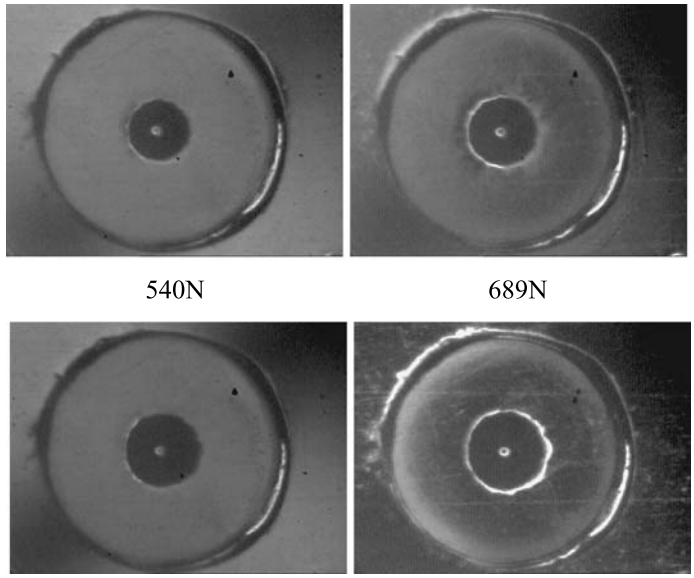


(a) Typical in-situ contact radius measurement for IN783 superalloy

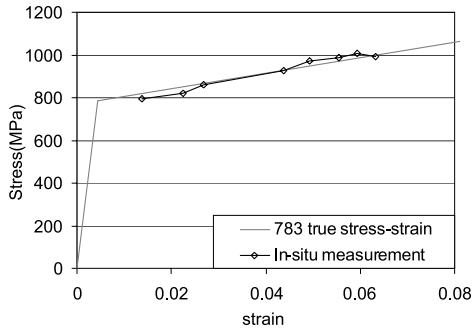


(b) Post-yielding stress-strain data compared with true stress-strain curve

equation (25) shows that the carrier effect can be automatically canceled out if elastic recovery is averaged in four center symmetric directions. An example is shown in Fig. 8(c), where using the above mentioned procedure, the carrier fringes were removed.

## Elastic Recovery and Young's Modulus

Figure 9(a) shows typical fringe pattern at a loaded state, where the outer white-lined circle denotes the indenter boundary. Figure 9(b) shows the corresponding phase map. Figure 9(c) is used to measure the contact radius. Figure 9(d) shows fringe patterns after unloading and Fig. 9(e) shows the corresponding phase map. Figure 9(f) shows the residual indent after unloading. No noticeable change of the contact radius was found between loaded and unloaded states. The phase map was first unwrapped to make it continuous, and then convert to displacement. As shown in Fig. 10(a), elastic recovery was calculated by subtracting the loaded and unloaded displacements. Using equation (7), elastic recovery was changed to $\Delta w \sim t$ relation as shown in Fig. 10(b) and (c) for flat-end punch model and spherical indentation model, respectively. The linear portion was chosen to calculate the slope $m$. The corresponding region was marked in Fig. 10(a). Young's modulus was then calculated based on equation (9). Results are shown in Table 3.

Figure 11 shows the loaded and unloaded fringe patterns, phase maps and contact radius images of one indentation for Al6061-T0. The apparent carrier fringes were automatically canceled out by averaging the elastic recovery in four center-symmetric directions. Figure 12(a) shows the elastic recovery plot. For the $\Delta w \sim t$ plots shown in Fig. 12(b) and (c), the linear portion was identified and corresponding region was marked in Fig. 12 using vertical dashed lines. Table 3 shows error percentage for the Young's modulus calculation.

**Fig. 14.** Post-yielding results for Al6061-T0

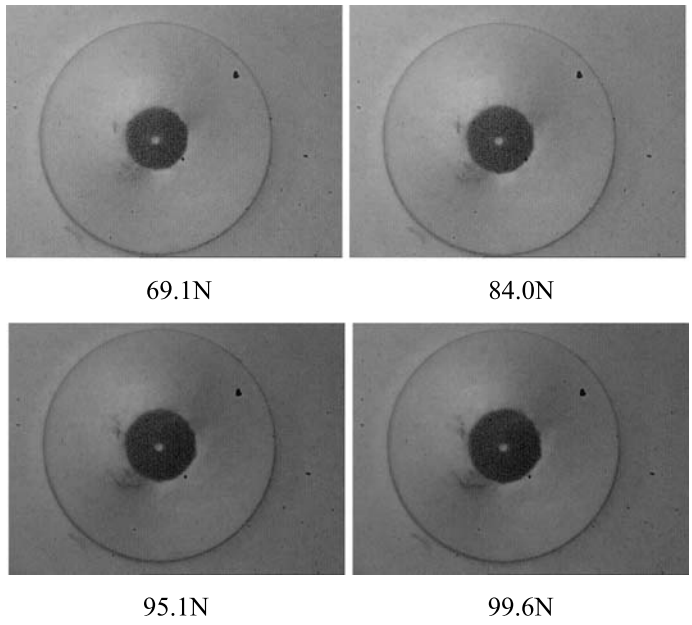


(a) Typical in-situ contact radius measurement for Al6061-T0 alloy

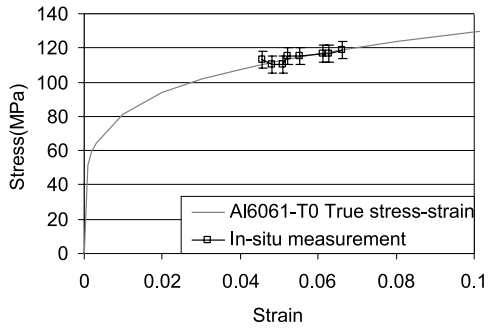


(b) Post-yielding stress-strain data compared with true stress-strain curve

Contact Radius Measurement for Post-Yielding Stress-Strain Determination

After the Young's modulus measurement, a sequence of monotonically increasing loads was applied at the same indented location. *In-situ* contact radius measurements were conducted to determine post-yielding stress-strain data using equation (1).

For steel and copper alloy, C = 2.8 was used by Tabor [1] with excellent correlation. However, in general, it was found to be strain hardening dependent, as discussed by Taljat [7]. Figure 13(a) shows the *in-situ* contact radius measurement of IN783 superalloy with increasing loads. Figure 13(b) shows the post-yielding stress-strain data using C = 2.9. Figure 14(a) shows the *in-situ* contact radius measurement of Al6061-T0 alloy with increasing loads and Fig. 14(b) shows the comparison between indentation stress-strain and true stress-strain with C = 2.8. Good agreement is noticed.

## Conclusions and Discussions

An *in-situ* Transparent Indenter Measurement (TIM) method was developed. Using the TIM method, Young's modulus and post-yielding stress and strain data can be measured through measured surface out-of-plane displacements and contact radii. Testing results of IN783 and Al6061-T0 alloys showed good agreement with known material properties. Finite element analyses also confirmed elastic recovery is a valid approach to determine the Young's modulus using either flat-end punch or spherical indentation. A method of automatically eliminating carrier fringe

patterns was developed for the purpose of automatic operation of the TIM method.

**Acknowledgments** The work is supported in part by DOE EPSCoR Program under contracts DE-FG02-01ER45899 and by the Office of Fossil Energy, Advanced Research Materials (ARM) Program, DOE, under contract DE-AC05-00OR22725 managed by UT-Battelle, LLC.

## References

1. Tabor D (1951) The Hardness of Metals. Clarendon Press, Oxford.
2. Sneddon IN (1965) The relation between load and penetration in the axisymmetric Boussinesq problem for a punch of arbitrary profile. Int J Eng Sci 3:47–57.
3. Bulychev SI, Alekhin VP, Shorshorov MKh, Ternovskii AP, Shnyrev GD (1975) Determining Young's modulus from the indentor penetration diagram. Ind Lab 41(9): 1409–1412.
4. Loubet JL, Georges JM, Marchesini JM, Meille G (1984) Vicker's indentation curves of magnesium oxide (MgO). J Tribol 106(43).
5. Doerner MF, Nix WD (1986) A method for interpreting the data from depth-sensing indentation instruments. J Mater Res 1(4):601–609.
6. Oliver WC, Pharr GM (1992) An improved technique for determining hardness and elastic modulus using load and displacement sensing indentation experiments. J Mater Res 7(6):1564–1583.
7. Taljat B, Zacharia T (1998) New analytical procedure to determine stress-strain curve from spherical indentation data. Int J Solids Struct 35(33):4411–4426.
8. Bhattacharya AK, Nix WD (1988) Finite element simulation of indentation experiments. Int J Solids Struct 24(9): 881–891.
9. Bhattacharya AK, Nix WD (1988) Analysis of elastic and plastic deformation associated with indentation testing of thin films on substrates. Int J Solids Struct 24(12):1287–1298.
10. Komvopoulos K (1988) Finite element analysis of a layered elastic solid in normal contact with a rigid surface. J Tribol 110:477–485.
11. Komvopoulos K (1989) Elastic-plastic finite element analysis of indented layered media. J Tribol 111:430–439.
12. Kral ER, Komvopoulos K, Bogy DB (1993) Elastic-plastic finite element analysis of repeated indentation of a half-space by a rigid sphere. J Appl Mech 60:829–841.
13. Kral ER, Komvopoulos K, Bogy DB (1995) Finite element analysis of repeated indentation of an elastic-plastic layered medium by a rigid sphere, part I: surface results. J Appl Mech 62:20–28.
14. Kral ER, Komvopoulos K, Bogy DB (1995) Finite element analysis of repeated indentation of an elastic-plastic layered medium by a rigid sphere, part II: subsurface results. J Appl Mech 62:29–42.
15. Prchlik L, Pisacka J, Sampath S (2003) Deformation and strain distribution in plasma sprayed nickel-aluminum coating loaded by a spherical indenter. Mater Sci Eng A 360:264–274.
16. Chen H, Lin Q, Chen J, Yu Z, Zhao Y (2001) On plastic zone around an indentation during stress determination by impact indentation method. Trans China Weld Inst 22(5).
17. Yu Z, Zhao Y, Chen H (2001) Impacted indentation method of measuring residue stress. J Shenyang Arch Civ Eng Univ 17(3).
18. Kral ER, Komvopoulos K (1996) Three-dimensional finite element analysis of surface deformation and stresses in an elastic-plastic layered medium subjected to indentation and sliding contact loading. J Appl Mech 63:365–375
19. Nadai A (1931) Plasticity: A Mechanics of the Plastic State of Matter. McGraw-Hill Book Company, Inc.
20. Underwood JH (1973) Residual-stress measurement using surface displacements around an indentation. Exp Mech 13(9):373–380.
21. Szutkowska M (1999) Fracture toughness measurement of WC-Co hardmetals by indentation method. J Adv Mater 31(3).
22. Alcala J, Barone AC, Anglada M (2000) Source, influence of plastic hardening on surface deformation modes around Vickers and spherical indents. Acta Mater 48(13):3451–3464.
23. Haggag FM (1989) Field Indentation Microprobe for Structural Integraity Evaluation, U.S. Patent No. 4,852,397.
24. Fischer-Cripps AC (2000) Introduction to Contact Mechanics. Springer.
25. Johnson KL (1985) Contact Mechanics. Cambridge University Press.
26. Cloud G (2003) Optical methods in Experimental Mechanics, part 8: Michelson Interferometry. Exp Tech 25(5).
27. Kang BS-J, Skeen J, Perry K, Hung YY (1997) Crack tip displacement measurements using automated phase shift moiré interferometry, 1997 SEM spring conference on experimental mechanics, pp 311–312, Bellevue, WA.
28. Special Metals Corporation, http://www.specialmetals.com.
29. Feng C (2005). Development of a Transparent Indenter Measurement System and Indentation Analysis for Material Mechanical Property Evaluation, Dissertation, West Virginia University.